A Fabry-Perot Imaging Search for Lyman-alpha Emission in Quasar Absorbers at $z \sim 2.4$

Varsha P. Kulkarni[1]

Department of Physics and Astronomy, University of South Carolina, Columbia, SC 29208

Bruce E. Woodgate[1]

Code 681, Goddard Space Flight Center, Greenbelt, MD 20771

Donald G. York[1,2]

Department of Astronomy and Astrophysics, University of Chicago, Chicago, IL 60637

Deepashri G. Thatte and Joseph Meiring

Department of Physics and Astronomy, University of South Carolina, Columbia, SC 29208

Povilas Palunas[1]

McDonald Observatory, University of Texas, Austin, TX 78712

Edward Wassell[1]

St Thomas Aquinas College and the Catholic Univ. of America

ABSTRACT

We have carried out a deep narrow-band imaging survey of six fields with heavy-element quasar absorption lines, using the Goddard Fabry-Perot (FP) system at the Apache Point Observatory (APO) 3.5-meter telescope. The aim of these observations was to search for redshifted Ly-α emission from the galaxies underlying the absorbers at $z = 2.3 - 2.5$ and their companion galaxies. The 3 σ sensitivity levels ranged between 1.9×10^{-17} and 5.4×10^{-17} erg s^{-1} cm^{-2} in

[1]Visiting Astronomer, Apache Point Observatory, 3.5-meter telescope, owned and operated by the Astrophysical Research Consortium.

[2]Also, the Enrico Fermi Institute

observed-frame Ly-α flux. No significant Ly-α emitters were detected at $> 3\sigma$ level. The absence of significant Ly-α emission implies limits on the star formation rate (SFR) of 0.9-2.7 $M_\odot$ yr^{-1} per 2-pixel x 2-pixel region, if no dust attenuation is assumed. We compare our results with those from other emission-line studies of absorber fields and with predictions for global average SFR based on the models of cosmic chemical evolution. Our limits are among the tightest existing constraints on Ly-α emission from galaxies in absorber fields, but are consistent with many other studies. In the absence of dust attenuation, these studies suggest that SFRs in a large fraction of objects in the absorber fields may lie below the global mean SFR. However, it is possible that dust attenuation is responsible for the low emission line fluxes in some objects. It is also possible that the star-forming regions are compact and at smaller angular separations from the quasar than the width of our point spread function and, get lost in the quasar emission. We outline future observations that could help to distinguish between the various possibilities.

Subject headings: quasars: absorption lines; galaxies: evolution; cosmology: observations

1. INTRODUCTION

A great deal of progress has been made in the last decade in the studies of distant galaxies. The average star formation history of the Universe has also been estimated from emission properties of galaxies detected in deep imaging and redshift surveys such as the Canada-France Redshift Survey and the Hubble Deep Field (e.g., Lilly et al. 1996; Madau et al. 1996, 1998). A large population of bright galaxies with high star formation rates (SFRs) has been uncovered by means of the Lyman-break technique (e.g., Steidel et al. 1999). However, such flux-limited studies may not be adequate for investigating the evolution of normal galaxies, since such studies are biased toward the brighter or the more actively star forming galaxies. In principle, a less biased sampling of distant galaxies may be obtained by means of the absorption lines they superpose in the radiation from background quasars.

The presence of heavy-element absorption lines in quasar spectra preselects regions that have undergone some degree of star formation. There is nothing special about the lines of sight to the absorbers except for the convenient placement of background quasars, assuming that most of the absorbers are intergalactic material and not ejected material near the QSO at high, special relativistic velocities. Thus, it is very likely that these absorbers are surrounded by other galactic or protogalactic objects at the same redshifts. Thus in principle,

deep images of quasar absorber fields may reveal star-forming regions at high redshift.

Since a well-known signature of star forming galaxies is strong Ly-α or H-α emission, a natural strategy to look for the absorber galaxies or their companions is to search for the redshifted emission lines. Several previous studies have attempted to detect continuum and line emission from galaxies underlying quasar absorbers. At low redshifts, [O II] or [O III] emission has been detected in Mg II systems with narrow-band imaging (e.g., Yanny 1990; Yanny, York, & Williams 1990; Bergeron & Boisse 1991; Yanny & York 1992). Searches for low-z damped Lyman-alpha absorbers (DLAs) have often imaged, and sometimes spectroscopically confirmed, galaxies with various morphologies (spirals, irregulars, low surface brightness galaxies etc.–e.g., Steidel et al. 1994, 1995; LeBrun et al. 1997; Bowen et al. 2001; Cohen 2001; Turnshek et al. 2001). At high redshifts, however, it has been much more difficult to identify and study in detail the galaxies responsible for quasar absorption systems. There have been a few detections of Ly-α emission in quasar absorber fields (e.g. Lowenthal et al. 1991; Francis et al. 1996; Roche, Lowenthal, & Woodgate 2000). However, most other attempts to detect Ly-α emission from high-z intervening ($z_{abs} < z_{em}$) DLAs have produced either non-detections or weak detections (e.g. Smith et al. 1989; Hunstead et al. 1990; Lowenthal et al. 1995; Djorgovski et al. 1996). Most of the few confirmed Ly-α detections for high-redshift DLAs have been for absorbers with $z_{abs} \approx z_{em}$, which may differ from the cosmologically more interesting general population of DLAs with $z_{abs} < z_{em}$ (e.g. Warren & Moller 1996; Moller & Warren 1998; Fynbo et al. 1999). Most attempts to detect DLAs in H-α have either yielded non-detections or detected objects separated by large angular distances from the quasars, rather than objects close to quasar sightlines (see, e.g., Teplitz, Malkan, & McLean 1998; Bechtold et al. 1998; Mannucci et al. 1998, Bunker et al. 1999). These objects, while unlikely to be the absorbing galaxies themselves, are still interesting because they are likely to be companion galaxies in the same cluster as the absorber. A summary of previous attempts to detect high-z DLAs in emission is given by Kulkarni et al. (2000).

With the goal of obtaining a large sample of SFR estimates in the fields of high-redshift absorbers, we have started a Lyman-α imaging survey for absorbers at $2.3 < z < 2.6$ using a Fabry-Perot imager as a tunable narrow-band filter. Here we report our results for six fields with known heavy-element absorption systems. Sample selection, observations, and data reduction are described in section 2. The reduced images and photometry are presented in section 3. Section 4 presents a comparison of our results with previous studies of the same fields and with results of other Ly-α emitter studies. Section 4 also compares the SFR constraints from our study with the estimates from other emission-line searches for quasar absorber galaxies. A comparison with predictions based on global SFR models is also presented.

2.   OBSERVATIONS AND DATA REDUCTION

2.1.   Sample Selection

The blue and vis-broad etalons in the Goddard Space Flight Center (GSFC) Fabry Perot (FP) imaging system have optimum sensitivity and resolution in the wavelength range $\sim 4000 - 5000$ Å. We therefore restricted our search to the redshift range $2.3 < z < 3.1$. We searched the York et al. (1991) catalog of heavy-element quasar absorbers for absorbers with (i) $2.3 < z_{abs} < 3.1$ (ii) $z_{abs} < z_{em} - 0.6$ to avoid absorbers possibly associated with the quasars, and (iii) with well-detected mixed ionization species (Si II, Al II or O I in addition to C IV and/or Si IV). Six such objects were finally observed. Two of these six systems are DLAs, and one is a sub-DLA. In addition to these six systems, we also observed the well-studied field of the radio galaxy 53W002 containing Ly-α emitters at $z \approx 2.4$ (Pascarelle et al. 1996a, 1996b; Keel et al. 1999), as a calibration object. Table 1 lists the general properties of the objects observed.

2.2.   Observations

The FP instrument used for our observations has a choice of six Queensgate 50 mm diameter piezo-electrically driven, capacitance-stabilized etalons which can be tuned to any wavelength in the range 4000-10000 Å, and with resolution from 2.5 Å to 28 Å FWHM depending on the etalon and the wavelength. The system throughput including the CCD is 20% in the red and 5% in the blue. The instrument is used at the Nasmyth f/10.3 focus of the APO 3.5 m telescope. Behind the telescope focus a field lens and collimator lens collimate the light through the etalon and an order-sorting blocking filter, and a camera lens refocuses onto the CCD.

The camera has a STIS technology SITe 2048x2048 CCD with 21 μm pixels, 5 e$^-$ rms readout noise, MPP (inverted operation), minichannels, and a very high efficiency down to 3400 Å. The quantum efficiency is 82% at 4000 Å, 90% at 7000 Å and 53% at 9000 Å. This provides a large field of view, low noise, smooth bias levels, high charge transfer efficiency, and high sensitivity with UV, visible and IR etalons. The instrument can be controlled from the observatory control room via the Apache Point fiber optics communication system, or remotely over the internet, using command line control and a VNC GUI monitoring system.

The wavelength transmitted by an FP system is a function of the field angle. $\Delta\lambda = \lambda[1/(1 + (r/f)^2)]$, where f is the camera lens focal length, 200 mm, and r is the distance on the detector from the optical axis. At the APO f/10.3 Nasmyth focus, $\Delta\lambda \approx \lambda\left\{1 - [1/\{1 +\right.$

$(5.8 \times 10^{-4}\theta)^2\}]\Big\}$, with θ in arcseconds on the sky. For example, for $\lambda = 4100$ Å, $\theta = 90$ ″, $\Delta\lambda = 11.1$ Å. The effective monochromatic field of view depends on the tolerable fraction of the spectral width.

Table 2 lists the details of our observations. The observations were carried out primarily with the blue etalon during 9 runs between October 2000 and May 2004. The seeing varied between 1.0″ and 1.8″ FWHM. Conditions were not photometric for many of the nights. The narrow-band exposures were obtained setting the FP to the air wavelengths of the expected Ly-α emission lines at the absorber redshifts. In some cases, additional narrow-band exposures were also obtained with the vis-broad etalon at wavelength settings offset by 400 km s^{-1} redward of the absorber redshifts. The wavelength calibration was checked throughout using scans of lines from an Ar lamp. A temperature control program was run throughout to automatically keep the FP wavelength setting fixed by correcting for effects of temperature variations every five minutes. The FWHMs for the different fields were 5.6-14.7 Å, as measured from the width of the calibration lamp lines. A 2×2 binning was used, resulting in a plate scale of 0.366 ″ per binned pixel. The full circular field of view corresponds to $\sim 3.4'$ in diameter. Of course, given the variation in the central wavelength as a function of angle from the axis, the central $\approx 2.1'$ diameter region is sampled within ± 400 km s^{-1} of the central wavelength expected at the absorber redshift at 4100 Å.

Total narrow-band integration times were 320-600 minutes per field, split into 8-15 exposures of 40 minutes each. In addition, B-band exposures were obtained for all fields to sample the UV continuum near the Ly-α line. A pentagonal dither pattern was used to aid with flat-fielding and cosmic ray removal. Twilight sky flats were obtained for each wavelength setting. Standard star exposures were obtained for HZ44. Additionally, images of the 53W002 field were also used for photometric calibration.

2.3. Data reduction

Data reduction was carried out using standard IRAF tasks. The biases on each night were combined to get an average bias frame. The darks, flats and the object frames were corrected for the overscan region using the ccdproc task. All the images were trimmed to a size of 561 x 561 pixels or $3.4' \times 3.4'$, which contains the full field of view of the Fabry Perot. The darks, the flats and the object frames on each night were bias-corrected with the average bias corresponding to that night. The flat frames and the object frames were then dark-corrected with the combined dark for each night. The flat frames were combined using the flatcombine task to produce average flats corresponding to different wavelengths and filter settings. In some cases, twilight or dome flats were not available for a particular wavelength

and filter setting. In such cases, dark-corrected object frames were combined (with all objects removed) to create an average sky flat that was later used for flatfielding. Object frames for a particular wavelength and filter settings were flat fielded using the average flats in the same setting. Bias, dark and flat frames from other nights in the same season were used in a very few cases where they were not available on the same night. The IRAF task cosmicrays was used to remove cosmic rays from each object frame. A bad pixel mask was created for each image and the bad pixels were removed using the IRAF tasks ccdproc or fixpix.

To account for the varying degrees of extinction encountered over different nights, we carried out an empirical correction. The flux counts for unsaturated bright stars were measured in each image using the phot task in IRAF. The counts were corrected for images with different exposure times. For each star, the maximum value of counts f_{max}^j from different images was taken as an indicator of the unextinguished flux level of the jth star. The flux ratio for the jth star in the ith image f_{max}^j/f_i^j was then calculated for the best four or five stars in all images to estimate the extinction factors. The extinction factors thus derived for these four or five stars in each given image were then averaged to get an indication of the extinction for that image. Finally, each image was multiplied by this average empirical extinction factor to get an extinction corrected image.

All extinction-corrected images for each field and filter/wavelength setting were registered and shifted so as to match the coordinates of a reference star in all frames. This was done using the imexam, lintran and imshift tasks. Some images were rotated using the geomap and gregister tasks to match the coordinates of all stars in different images, to correct for a small rotational offset between some images taken at the same pointing in different observing seasons. Finally, the individual exposures for a given object and given wavelength and filter setting were combined using the IRAF task imcombine to get the final narrow-band and broad-band images.

3. RESULTS

Figures 1(a)-6(a) show $2.1' \times 2.1'$ sections of the reduced broad-band (B) images of the quasar absorber fields of Q0216+080, Q0636+680, Q0956+123, Q1209+093, Q1442+101, and Q2233+131, respectively. The corresponding panels (b) show the narrow-band images of the same fields obtained with the blue etalon. The stripes at the borders of some images are an artifact of the coadding of the dithered images. The quasar is absent or considerably dim in the narrow-band images for Q0216+080, Q1209+093, and Q2233+131 since the absorbers being studied in these systems are DLAs or sub-DLAs. Figure 7 shows the calibration field 53w002.

The expected B-band continuum must be subtracted from the observed narrow-band fluxes in order to determine if a statistically significant redshifted Ly-α excess exists for any object seen in both bands. We estimated the continuum in the narrow-band images by scaling the B images using the relative photometric calibrations of the two images. To do this, we subtracted a scaled B band image from the narrow-band image, aligning the images spatially, and adjusting the scaling factor so as to minimize variance in the central portion of the subtracted image. Furthermore, to minimize the effect of different seeing in the broad-band and narrow-band images, the broad and narrow-band images were convolved with a Gaussian of the same FWHM before subtraction in IDP3. The subtraction was carried out interactively, using the interactive data language (IDL, version 6.1) program Image Display Paradigm-3 (IDP-3) version 2.7, written by D. Lytle and E. Stobie (see, e.g., Lytle et al. 1999) Figs. 1(c)-7(c) show the resultant continuum-subtracted images for the six quasar absorber fields and the calibration field of 53w002. Finally, Figs. 1(d)-7(d) show $1' \times 1'$ close-up views of the continuum-subtracted images.

All of the objects in the narrow-band images disappeared almost completely after subtraction of the continuum. The slight residuals left at the positions of some objects arise because of the difficulty in matching the point spread functions (PSFs) perfectly in the broad and narrow-band images. No significant Ly-α emission at $> 3\sigma$ level was detected from any object in any of the quasar absorber fields. The few vis-B images obtained for three of the fields (Q0216+080, Q0636+680, Q2233+131) were also analyzed in a similar manner, and showed no Ly-α detections either. No significant objects were found even if the images were smoothed using Gaussian filters of about 2.5 or 5 pixels FWHM. Finally, we also compared our images with broad-band images from the Sloan Digital Sky Survey (SDSS) where available. A few very faint features are seen in our images for Q0216+080, but these features are indistinguishable from the noise. In Q0636+680 and Q0956+123, some residual flux is seen close to the quasar after continuum subtraction. However, these regions close to the quasars are not well sampled at our modest angular resolution. Thus, it is not clear whether the residuals seen near Q0636+680 and Q0956+123 are significant features or artifacts, without obtaining higher resolution images of these fields. In the case of Q0956+123, the feature apparent near the left upper corner of Fig. 3(d) is an artifact arising from a residual multipixel cosmic ray event in a single narrow-band image. In the field of Q2233+131, three bright galaxies are seen: $17.4''$ east and $1.7''$ south of the quasar; $28.2''$ east and $51.7''$ south of the quasar; and $35.2''$ east, $30.2''$ north of the quasar (Fig. 6c). All of these galaxies are seen in the SDSS. However, all of these galaxies are far too bright to be at $z = 2.55$ ($g = 19.76, 20.35, 20.49$ respectively from SDSS). It is more likely that the excess emission seen in these objects is [O II] $\lambda 3727$ emission from interloper galaxies at $z = 0.16$. We plan to obtain spectra of these galaxies in the near future to determine their redshifts.

To estimate the limits on the Ly-α fluxes for the absorbers in our fields, we used our calibration observations of the field of the radio galaxy 53w002. This field is known to have Ly-α emitters at $z = 2.39$ (Pascarelle et al. 1996a, 1996b; Keel et al. 1999). For calibration purposes, we used the brightest objects seen in our continuum-subtracted narrow-band images of this field, i.e., objects 3 and 1 of Keel et al. (1999; table 2), labeled O1 and O2 in the bottom panel of Figure 7. Aperture photometry of these two objects was carried out using the IRAF task phot with aperture sizes ~ 3 times the seeing FWHM. Using the Ly-α fluxes for these from Table 2 of Keel et al. (1999) and the counts measured for those objects in our images, we estimated the photometric calibration of our images. To correct for sensitivity differences at the different wavelengths used for our quasar absorbers and the calibration field 53w002, we used our observations of standard star HZ44. Using the photometry of this star in images obtained at the different wavelength settings, and adopting the absolute spectral distribution of this star from Oke (1990), we estimated the relative sensitivity differences of the FP at the different wavelengths.

We next estimated the noise level in the continuum-subtracted blue-etalon images for each field. To do this, we considered a $10'' \times 10''$ region centered on the quasar and determined the noise profile over this region using IDP-3. While doing this, we disregarded a circular region centered on the quasar with a radius of roughly twice the seeing FWHM to avoid effects of imperfect seeing matches between the broad and narrow band images. We then measured the mean noise level per pixel in concentric annuli of radii ranging from 2 times the seeing to 5 $''$, and finally corrected for the sensitivity differences at the various wavelengths. The noise level per pixel was found to be nearly constant everywhere (within a few %) in this region. The mean value of the noise per pixel was used to estimate the noise level per 2 pixel x 2 pixel region, assuming Poisson statistics. Based on this, we estimated the 3 σ observed-frame Ly-α point source flux sensitivity reached in our images. If dust attenuation is assumed to be small, these Ly-α flux limits can be converted to limits on the star formation rates (SFRs). These point-source SFR limits implied by the non-detections of Ly-α emission in our quasar absorber fields are listed in Table 3 and are in the range of 0.9-2.7 $M_\odot$ yr^{-1}. Here, we have used the prescription of Kennicutt (1998) for converting H-α luminosity $L_{H-\alpha}$ to the SFR, i.e., $SFR(M_\odot \, yr^{-1}) = 7.9 \times 10^{-42} L(H-\alpha)(erg \, s^{-1})$ and assumed a ratio $L_{Ly-\alpha}/L_{H-\alpha} = 8.7$ for case-B recombination.

We also used our continuum-subtracted images to estimate the flux limits for a diffuse foreground absorbing galaxy. To do this, we used the mean value of the noise per pixel to estimate the flux limit over the entire $10'' \times 10''$ region. This flux limit was used to calculate the limiting Ly-α luminosity and hence the limiting SFR in the $10'' \times 10''$ region. At $z = 2.4$, this region corresponds to a size of $\approx 81 \times 81$ kpc^2 centered on the quasar, for the comsology adopted here. The diffuse-source flux limits are in the range of 2.6-7.4 $\times 10^{-16}$ erg s^{-1} cm^{-2}

summed over the $10'' \times 10''$ region. The corresponding summed SFR limits are in the range of 12.3-36.4 $M_\odot$ yr^{-1} over the entire $10'' \times 10''$ region.

4. DISCUSSION

4.1. Comparison with Other Imaging Studies of Our Targets

For most of our targets, no other imaging information exists in any waveband on a scale comparable to our fields of view. For Q0216+080 and Q2233+131, HST NICMOS H-band images are available (Warren et al. 2001). The NICMOS images of Q0216+080 show two objects with $H_{AB} = 25.75$ and 24.34, located $1.4''$ and $3.8''$ away from the quasar, at position angles of -104.8 and 97.8 degrees east of north, respectively. However, the closer object is likely to be an artifact since it occurs on a diffraction spike. For Q2233+131, the NICMOS H-band image revealed two objects with $H_{AB} = 25.05$ and 25.12, located $2.8''$ and $3.3''$ away from the quasar, at position angles of 158.6 and 68.3 degrees east of north, respectively. Of these, the former object has been identified with a Lyman limit system at $z = 3.15$ (Djorgovski et al. 1996). None of these objects are seen in our B-band or NB images. This could be because of the difference in angular resolutions of our study and the NICMOS study. In either case, no information on star-forming emission-line objects is available from these broad-band images. The only additional emission-line constraints available are for Q0216+080 and Q2233+131. The narrow-band imaging study of Deharveng et al. (1990) found no Ly-α emitters in the Q0216+080 field, placing a 3 σ upper limit of 6.9×10^{-16} erg s^{-1} cm^{-2} on the Ly-α emission flux. Our observations of this field have provided a Ly-α flux limit > 10 times tighter than that of Deharveng et al. (1990). For Q2233+131, our limit agrees closely (within $\approx 20\%$) with that of Lowenthal et al. (1995).

4.2. The Space Density of Ly-α Emitters: Comparison with Other Studies

To understand whether the non-detections of Ly-α emitters (LAEs) in our fields are consistent with other surveys for Ly-α emitters, we now examine results from some recent LAE searches. Stiavelli et al. (2001) detected 58 LAE candidates over a field of 1200 arcmin^2 at $z = 2.422 \pm 0.072$. Based on this, they deduced a completeness-corrected space density of 0.07 LAEs per arcmin^2 with Ly-α fluxes above 2×10^{-16} erg cm^{-2} s^{-1}. Palunas et al. (2004) detected 37 absorbers in a 46' $\times$ 46' field of view. Based on this, they derived the space density of LAEs to be 0.019 arcmin^{-2} in a redshift interval $\Delta z = 0.045$ at $z \sim 2.4$. These (Stiavelli et al. 2001, Palunas et al. 2004) studies imply 0.49 and 0.42 LAEs per arcmin^2 per

unit redshift, respectively. At $z = 4.5$, LAE searches by Rhoads et al. (2000) and Malhotra & Rhoads (2002) have found space densities of 4000 deg^{-2} per unit redshift, i.e. 1.1 LAE per arcmin^2 per unit redshift.

These other LAE searches cover much wider fields of view, and larger redshift ranges Δz (wider filter bandwidths) than our study. Adopting a mean space density of 0.45 LAEs per arcmin^2 per unit redshift at $z = 2.4$ from Stiavelli et al. (2001) and Palunas et al. (2004), and using $\Delta z \approx 0.003$ as a typical redshift range covered by our study, one would expect < 1 absorber in our fields with effective monochromatic coverage of $\approx 2.1'$, if our fields were similar to the other LAE fields.

On the other hand, the LAE searches of Rhoads et al. (2000), Stiavelli et al. (2001), and Malhotra & Rhoads (2002) are not selected by the presence of a quasar absorption system. The presence of a well-established heavy-element quasar absorber with mixed ionization implies the existence of a region that has had some star formation. At $z \sim 2.4$, our complete fields of view of about 3.4' diameter cover about 2.2 Mpc^2 around the absorbing sightline (assuming $\Omega_m = 0.3$, $\Omega_\Lambda = 0.7$, and $H_0 = 70$ km s^{-1} Mpc^{-1}). Given the gradient in the central wavelength, the roughly monochromatic (within ± 400 km s^{-1} of the absorber) fields of view of about 2.1' diameter cover about 0.8 Mpc^2 around the quasar sightline. Since the absorbing galaxy certainly must lie within this region, one might expect a higher LAE density in our fields than that in a blind field. Francis et al. (1996, 2004) and Palunas et al. (2004) did indeed find a number of LAEs in wide-field surveys surrounding a field with 3 sub-DLAs. However, this region appears to be a filament with higher density than a typical field region. Furthermore, the LAEs in this filament are separated from 2 of the 3 absorber sightlines by more than 2' in radius (see Fig. 4 of Palunas et al. 2004). Such objects would thus not be detectable in a field of view such as ours. Thus, overall, the lack of LAEs in our observations are not inconsistent with the space density of LAEs found by other studies. We note, however, that detailed comparisons would require a full consideration of the luminosity function of LAEs since our observations reach fainter flux limits than many of the other LAE searches.

4.3. The Star Formation Rates of Quasar Absorbers and their Companions

Fig. 8 plots our SFR limits in the fields of quasar absorbers together with the results of other searches for Ly-α, H-α, H-β, [O II], and [O III] emission in quasar absorber fields. The filled red triangles show our APO Ly-α limits, while the unfilled black triangles at $z \approx 1.9$ show our limits from previous H-α imaging with HST/NICMOS (Kulkarni et al. 2000, 2001). Other data are from Yanny et al. (1987); Yanny, York, & Williams (1990); Yanny (1990);

Hunstead et al. (1990); Deharveng et al. (1990, 1995); Giavalisco et al. (1994); Lowenthal et al. (1995); Francis et al. (1996); Warren & Móller (1996); Bergvall et al. (1997); Mannucci et al. (1998); Teplitz et al. (1998); Bunker et al. (1999); Fynbo et al. (1999, 2000); Bouche et al. (2001); van der Werf et al. (2000); Móller et al. (2002); Meyer, Thompson, & Mannucci (2003); Móller, Fynbo, & Fall (2004); Christensen et al. (2004, 2005); Schulte-Ladbeck et al. (2004); Chen, Kennicutt, & Rauch (2005); and Weatherley et al. (2005). In total, we have plotted 71 detections and 30 upper limits in Fig. 8. We note, however, that many of the emission line detections are for candidates that have not yet been confirmed with spectroscopy or multiple narrow-band imaging. For the few objects where multiple emission lines have been detected, we have plotted the values from H-α, H-β, or [O II], in that order of preference. All the shown candidate detections and $3\,\sigma$ upper limits have been normalized to $\Omega_m = 0.3$, $\Omega_\Lambda = 0.7$, and $H_0 = 70$ km s^{-1} Mpc^{-1}. Once again, the prescription of Kennicutt (1998) has been used for the conversion from the H-α luminosity $L_{H-\alpha}$ to the SFR, and a ratio $L_{Ly-\alpha}/L_{H-\alpha} = 8.7$ for case-B recombination has been assumed. No correction has been made for dust attenuation, but we examine this issue in more detail below. Our APO FP constraints are among the lowest, but are clearly consistent with many other measurements. The open inverted triangles at $0 < z < 2.5$ are based on spectroscopic (slit) observations of H-α. The unfilled circles are candidate objects with H-α emission detected at the absorber redshift, but are often more than $\sim 10''$ away from the quasar, and have a lower precision in redshift.

The curves in Fig. 8 are useful for comparing the data with global predictions based on the luminosity density of galaxies from the deep galaxy imaging surveys. Since most of the data in Fig. 8 are for objects in DLA fields, we show the calculations of Bunker et al. (1999) for the predicted cross-section-weighted SFR in DLAs. These models use two alternative sets of assumptions about the number of absorbers per unit redshift and the distribution of global SFR among individual absorbers at a given redshift. The thick and thin solid curves show the LD5 and LD0 "large disk" calculations (for $q_0 = 0.5$ and $q_0 = 0$ respectively), of Bunker et al. based on the closed-box Pei & Fall (1995) models. The LD models assume that DLAs are the progenitors of spiral galaxies, with space density equal to that of local spirals, but with size and SFR of each DLA larger in the past compared to that of a local spiral. The dashed curve shows the H5 and H0 predictions of Bunker et al. (1999) (for $q_0 = 0.5$ and $q_0 = 0$ respectively) for the "hierarchical" hypothesis, which assumes that there were multiple DLAs at high redshift corresponding to every present-day spiral (i.e. that DLAs were sub-galactic fragments that later merged to form present-day spirals). Thus in the H5 and H0 models, DLAs have the same distribution of gas cross-section sizes as in local spirals, but with a higher space density in the past, and have smaller SFRs than in the corresponding "large-disk" models.

The LD curve, if computed for $\Omega_m = 0.3$, $\Omega_\Lambda = 0.7$, and $H_0 = 70$ km s^{-1} Mpc^{-1}, would lie between the LD5 and LD0 curves, since the distance and time scales for the former cosmology are intermediate between those for $q0 = 0$ and $q0 = 0.5$. This can also be seen by comparing the comoving global SFR predicted by the Pei & Fall (1995) closed-box models for $q_0 = 0.5$ and $q_0 = 0$, with that predicted by the Λ-cold dark matter (Λ-CDM) hydrodynamical simulations of Nagamine, Cen, & Ostriker (2000). Thus, a large fraction of the observed SFRs would appear to fall significantly below the prediction of the large-disk scenario. The H curve for this Λ-CDM cosmology would be identical to the H5 and H0 curves (since the latter curves coincide with each other). A large fraction of the data points in Fig. 8 thus appear to be more consistent with the hierarchical scenario, suggesting perhaps that many absorbers or their companion galaxies may be arising in star-forming dwarf galaxies or sub-galactic fragments that merged later to form present-day galaxies. However, several detections and upper limits, including our FP limits, appear to be considerably below even the hierarchical prediction. Indeed, about 63% of the detections and about 73% of the limits plotted in Fig. 8 are less than 5 $M_\odot$ yr^{-1}. Such large local deviations for the absorber fields from the global mean would be surprising.

Taken at face value, Fig. 8 suggests that the absorption-based view of the cosmic star formation history could be quite different from the emission-based view, i.e., from the star formation history inferred on the basis of the direct galaxy imaging surveys such as the Hubble Deep Field. Low SFRs for galaxies in absorber fields would also be consistent with the low global metallicities found in DLAs (e.g., Kulkarni et al. 2005 and references therein). Similar suggestions have also been made by Wolfe et al. (2003), who inferred relatively high SFR values for some DLAs based on C II* absorption, but found the high SFRs to be inconsistent with the low metallicities observed in the DLAs. We note, however, that while the C II* method may potentially offer an interesting way to estimate SFRs in DLAs, it seems less direct and more model-dependent than the emission-line based constraints.

There are also other possible interpretations of Fig 8. It is possible that the true SFRs in galaxies in the absorber fields are higher, but their emission lines, especially Ly-α, are attenuated by dust. It is well known that resonance scattering of Ly-α, in the presence of dust, can lead to quenching of the Lyman-α emission in high-$N_{\rm HI}$ systems (e.g., Charlot & Fall 1991). Presence of dust in some Ly-α emitting regions is also suggested from the recent detection of 24 μm emission in Spitzer Space Telescope images of LAEs at $z = 2.4$ in an absorber field (Colbert et al. 2004). On the other hand, there are several reasons to expect that Ly-α emission may still be seen from absorbers and their companion galaxies, in at least some cases. First, the very knowledge of a DLA means that the quasar in which it appears is not greatly affected by dust attenuation. Ly-α is easily seen from regions of such low extinction. Second, the dust-to-gas ratios in DLAs inferred from relative abundances

such as [Cr/Zn] or [Fe/Zn] are much smaller than in the Milky Way (e.g., Pettini et al. 1997; Khare et al. 2004; and references therein). In a recent study of a large number of SDSS quasar spectra, we have recently found evidence for a statistically significant but small amount of dust in quasar absorbers (York et al. 2005). Finally, there are several examples of high-z Ly-α emitters with very little dust attenuation (e.g., Giavalisco et al. 1994; Francis et al. 1996; Hu, Cowie, & McMahon 1998; Kudritzki et al. 2000).

The effect of dust attenuation is expected to be much less severe in the H-α line. Indeed, the SFR constraints based on H-α detections in most high-z DLA candidates or companions shown in Fig 8 are considerably higher than the constraints from the Ly-α emission searches. Considering detections alone, the median SFRs from H-α, Ly-α, and [OII] are 35.9, 3.2, and 0.3 $M_\odot$ yr^{-1}, respectively. If both detections and limits are considered, the median SFRs from H-α, Ly-α, and [OII] are 28.2, 2.4, and 0.3 $M_\odot$ yr^{-1} treating the limits as detections, and 18.8, 0.1, and 0.3 $M_\odot$ yr^{-1} treating the limits as zeros. It is tempting to think that the difference between the median H-α and Ly-α values could be partly caused by dust extinction. However, it is not clear whether this is a significant effect, since Ly-α measurements (candidates or limits) are not available for most of the H-α candidates. In the few objects that show detections of multiple emission lines, the SFR estimates from the available lines are usually consistent within a factor of ~ 2. Also, some of the H-α candidates are at large angular separations from the quasars and have less accurate redshifts. Thus, there is no clear indication that Ly-α in the H-α candidates is attenuated by dust. In any case, dust alone may not explain low Ly-α emission in every individual case, because the extent of Ly-α attenuation also depends on several other factors, such as the orientation, the topology of the H II region, and the distribution of stars, gas and dust within the absorber. Finally, dust attenuation cannot explain why nearly all of the SFRs inferred from [O II] and $\approx 25\%$ of the SFRs inferred from H-α are low.

Another possibility is that the star-forming regions in the absorber galaxies are compact, lie directly in front of the quasars, and hence get lost in the quasar point spread function (PSF) in our study and other ground-based studies so far. For example, if the absorbing galaxies had star-forming cores comparable in size to those in the Lyman-break galaxies [typically $\sim 1.6\,(H_0/70)^{-1}$ kpc] aligned perfectly in front of the quasars, it would not be possible to resolve them with studies such as our own (and most other ground-based studies used in Fig. 8). In other words, the SFR constraints derived from such studies may be more appropriate for the companion galaxies of the absorbers, rather than the absorbers themselves. It is difficult to rule out this possibility without high-resolution imaging data. However, the chance of having the star forming region exactly in front of the quasar in *each* case is small. Indeed, the absence of emission within the Ly-α absorption profiles in the published spectra for most DLAs (including those from our study) suggests that they do

not have star-forming regions perfectly aligned with the background quasars. Even if the absorber galaxies themselves were small, they are unlikely to be isolated objects, since such small galaxies are expected to occur as companions to larger galaxies within a few hundred kpc. In any case, it would still be surprising why the few existing high-resolution imaging studies of absorber galaxies have often failed to detect H-α emission or found relatively weak Ly-α emission (e.g., Bouche et al. 2001; Kulkarni et al. 2000, 2001; Móller et al. 2002).

Future narrow-band imaging studies of more high-redshift quasar absorber fields would help to understand whether the low Ly-α fluxes we find are representative of the absorber galaxies. Furthermore, more narrow-band imaging or spectroscopic studies in the near-infrared will give access to the H-α emission line from the $z \sim 2.5$ absorbers. A systematic comparison of the H-α and Ly-α data for the same absorbers can help to understand whether the emission lines in the galaxies in absorber fields are simply attenuated by dust, or whether these galaxies truly have low SFRs. It will thus be interesting to look at Ly-α emission from the objects reported to show strong H-α emission, and to look at H-α near the quasars for which we have limits on Ly-α. Finally, more high-resolution narrow-band imaging and/or spectroscopic studies would be especially important to understand whether the star formation in the absorber galaxies is restricted to compact regions.

REFERENCES

Bechtold, J., Elston, R., Yee, H. K. C., Ellingson, E., & Cutri, R. M. 1998, in 'The Young Universe: Galaxy Formation and Evolution at Intermediate and High Redshift', ed. S. D'Odorico, A. Fontana, and E. Giallongo, ASP Conf. Series, (PASP), 146, 241

Bergeron, J. & Boissé, P. 1991, A&A, 243, 344

Bergvall, N., Ostlin, G., Karlsson, K. G., Orndahl, E., & Ronnback, J. 1997, A&A, 321, 771

Bouche, N., Lowenthal, J. D., Charlton, J. C., Bershady, M. A., Churchill, C. W., & Steidel, C. C. 2001, ApJ, 550, 585

Bowen, D. V., Tripp, T. M., & Jenkins, E. B. 2001, AJ, 121, 1456

Bunker A., J., Warren, S. J., Clements, D. L., Williger, G. M. & Hewett, P. C. 1999, MNRAS, 309, 875

Charlot, S., & Fall, S. M. 1991, ApJ, 378, 471

Chen, H.-W., Kennicutt, R. C., & Rauch, M. 2005, ApJ, 620, 703

Christensen, L., Sanchez, S. F., Jahnke, K., Becker, T., Wisotzki, L., Kelz, A., Popovic, L. C., & Roth, M. M. 2004, A&A, 417, 487

Christensen, L., Schulte-Ladbeck, R. E., Sanchez, S. F., Becker, T., Jahnke, K., Kelz, A., Roth, M. M., & Wisotzki, L. 2005, A&A, 429, 477

Cohen, J. G. 2001, AJ, 121, 1275

Colbert, J., Teplitz, H., Williger, G., Palunas, P., Woodgate, B., & Francis, P. 2004, BAAS, 205, 63.11

Deharveng, J. M., Bowyer, S., & Buat, V 1990, A&A, 236, 351

Deharveng, J.-M., Buat, V., & Bergeron, J. 1995, A&A, 298, 57

Djorgovski, S. G., Pahre, M. A., Bechtold, J., & Elston, R. 1996, Nature, 382, 234

Francis, P. J. et al. 1996, ApJ, 457, 490

Francis, P., Palunas, P., Teplitz, H. I., Williger, G. M., & Woodgate, B. E. 2004, ApJ, 614, 75

Fynbo, J. U., Móller P., & Warren, S. J. 1999, MNRAS, 305, 849

Fynbo, J. U., Thomsen, B., Móller P. 2000, A&A, 353, 457

Giavalisco, M., Macchetto, F. D., & Sparks, W. B. 1994, A&A, 288, 103

Hu, E. M., Cowie, L. L., & McMahon, R. G. 1998, ApJ, 502, L99

Hunstead, R. W., Pettini, M., & Fletcher, A. B. 1990, ApJ, 365, 23

Keel, W. C., Cohen, S. H., Windhorst, R. A., & Waddington, I. 1999, AJ, 118, 2547

Kennicutt, R. C. 1998, ARAA, 36, 189

Khare, P., Kulkarni, V. P., Lauroesch, J. T., York, D. G., Crotts, A. P. S., & Nakamura, O. 2004, ApJ, 616, 86

Kudritzki, R.-P. et al. 2000, ApJ, 536, 19

Kulkarni, V. P., Hill, J. M., Schneider, G., Weymann, R. J., Storrie-Lombardi, L. J., Rieke, M. J., Thompson, R. I., & Jannuzi, B. 2000, ApJ, 536, 36

Kulkarni, V. P., Hill, J. M., Schneider, G., Weymann, R. J., Storrie-Lombardi, L. J., Rieke, M. J., Thompson, R. I., & Jannuzi, B. 2001, ApJ, 551, 37

Kulkarni, V. P. & Fall, S. M. 2002, ApJ, 580, 732

Kulkarni, V. P., Fall, S. M., Lauroesch, J. T., York, D. G., Welty, D. E., Khare, P., Truran, J. W. 2005, ApJ, 618, 68

Le Brun, V., Bergeron, J., Boisse, P., & Deharveng, J.-M. 1997, A&A, 321, 733

Lilly, S. J., Le Fevre, O., Hammer, F., & Crampton, D. 1996, ApJ, 460, L1

Lowenthal, J. D., Hogan, C. J., Green, R. F., Caulet, A., Woodgate, B., Brown, L., & Foltz, C. B. 1991, ApJ, 377, L73

Lowenthal, J. D., Hogan, C. J., Green, R. F., Woodgate, B., Caulet, A., Brown, L., & Bechtold, J. 1995, ApJ, 451, 484

Lytle, D., Stobie, E., Ferro, A., & Barg, I., 1999, ASP Conf. Ser. 172, Astronomical Analysis Software and Systems 8, ed. D. Mehringer, R. Plante & D. Roberts (San Francisco: AP), 445

Madau, P., Ferguson, H. C., Dickinson, M. E., Giavalisco, M., Steidel, C. C., & Fruchter, A. 1996, MNRAS, 283, 1388

Madau, P., Pozzetti, L., & Dickinson, M. 1998, ApJ, 498, 106

Malhotra, S. & Rhoads, J. E. 2002, ApJ, 565, L71

Mannucci, F., Thompson, D., Beckwith, S. V. W., & Williger, G. M. 1998, ApJ, 501, L11

Meyer, R., Thompson, D. & Mannucci, F. 2003, ApJ, 585, 73

Móller, P., & Warren, S. J. 1998, MNRAS, 299, 661

Móller, P., Fynbo, J. P. U., & Fall, S. M. 2004, A&A, 422, L33

Móller, P., Warren, S. J., Fall, S. M., Fynbo, J. U., & Jakobsen, P. 2002, ApJ, 574, 51

Nagamine, K., Cen, R., & Ostriker, J. P. 2000, ApJ, 541, 25

Oke, J. B. 1990, AJ, 99, 1621

Palunas, P., Teplitz, H. I., Francis, P. J., Williger, G. M., & Woodgate, B. E. 2004, ApJ, 602, 545

Pascarelle, S. M., Windhorst, R. A., Keel, W. C., & Odewahn, S. C. 1996a, Nature, 383, 45

Pascarelle, S. M., Windhorst, R. A., Driver, S., Ostrander, E., & Keel, W. 1996b, ApJ, 456, L21

Pei, Y. C. & Fall, S. M. 1995, ApJ, 454, 69

Pei, Y. C., Fall, S. M., & Hauser, M. G. 1999, ApJ, 522, 604

Pettini, M., King, D. L., Smith, L. J. & Hunstead, R. W. 1997, ApJ, 478, 536

Rhoads, J. E., Malhotra, S., Dey, A., Stern, D., Spinrad, H., & Jannuzzi, B. T. 2000, ApJ, 545, L85

Roche, N., Lowenthal, J. & Woodgate, B. 2000, ApJ, 317, 937

Schulte-Ladbeck, R. E., Rao, S. M., Drozdvosky, I. O., Turnshek, D. A., Nestor, D. B., & Pettini, M. 2004, ApJ, 600,613

Smith, H. E., Cohen, R. D., Burns, J. E., Moore, D. J., & Uchida, B. A. 1989, ApJ, 347, 87

Steidel, C. C., Pettini, M., Dickinson, M., & Persson, S. E. 1994, AJ, 108, 2046

Steidel, C. C., Bowen, Blades, & Dickinson, M. 1995, ApJ, 440, L45

Steidel, C. C., Adelberger, K. L., Giavalisco, M., Dickinson, M., & Pettini, M. 1999, ApJ, 519, 1

Stiavelli, M., Scarlata, C., Panagia, N., Treu, T., Bertin, G., & Bertola, F. 2001, ApJ, 561, L37

Teplitz, H. I., Malkan, M., & McLean, I. S., 1998, ApJ, 506, 519

Turnshek, D. A., Rao, S., Nestor, D., Lane, W., Monier, E., Bergeron, J. & Smette, A. 2001, ApJ, 553, 288

van der Werf, P. P., Moorwood, A. F. M., & Bremer, M. N. 2000, A&A, 362, 509

Warren, S. J., & Móller, P. 1996, A&A, 311, 25

Weatherley, S. J., Warren, S. J., Moller, P., Fall, S. M., Fynbo, J. U., & Croom, S. M. 2005, MNRAS, 358, 985

Wolfe, A. M., Gawiser, E., & Prochaska, J. X. 2003, ApJ, 593, 235

Yanny, B. 1990, ApJ, 351, 396

Yanny, B., York, D. G., Hamilton, D., Schommer, R. A., & Williams, T. V. 1987, ApJ, 323, L19

Yanny, B., York, D. G., & Williams, T. B. 1990, ApJ, 351, 377

Yanny, B., & York, D. G. 1992, ApJ, 391, 569

York, D. G.; Yanny, B.; Crotts, A.; Carilli, C.; Garrison, E.; Matheson, L. 1991, MNRAS, 250, 24

York, D. G. et al. 2005, MNRAS, to be submitted

FIG. 1– *APO images of the field of Q0216+080. (a) $2.1' \times 2.1'$ B-band image (top left); (b) $2.1' \times 2.1'$ narrow-band image before continuum subtraction (top right); (c) $2.1' \times 2.1'$ narrow-band image after continuum subtraction (bottom left); and (d) $1' \times 1'$ narrow-band image after continuum subtraction (bottom right). See attached gif images.*

FIG. 2– *Same as for Fig. 1, for the field of Q0636+680.*

FIG. 3– *Same as for Fig. 1, for the field of Q0956+123.*

FIG. 4– *Same as for Fig. 1, for the field of Q1209+093.*

FIG. 5– *Same as for Fig. 1, for the field of Q1442+101.*

FIG. 6– *Same as for Fig. 1, for the field of Q2233+131.*

FIG. 7– *Same as for Fig. 1, for the calibration field of 53w002.*
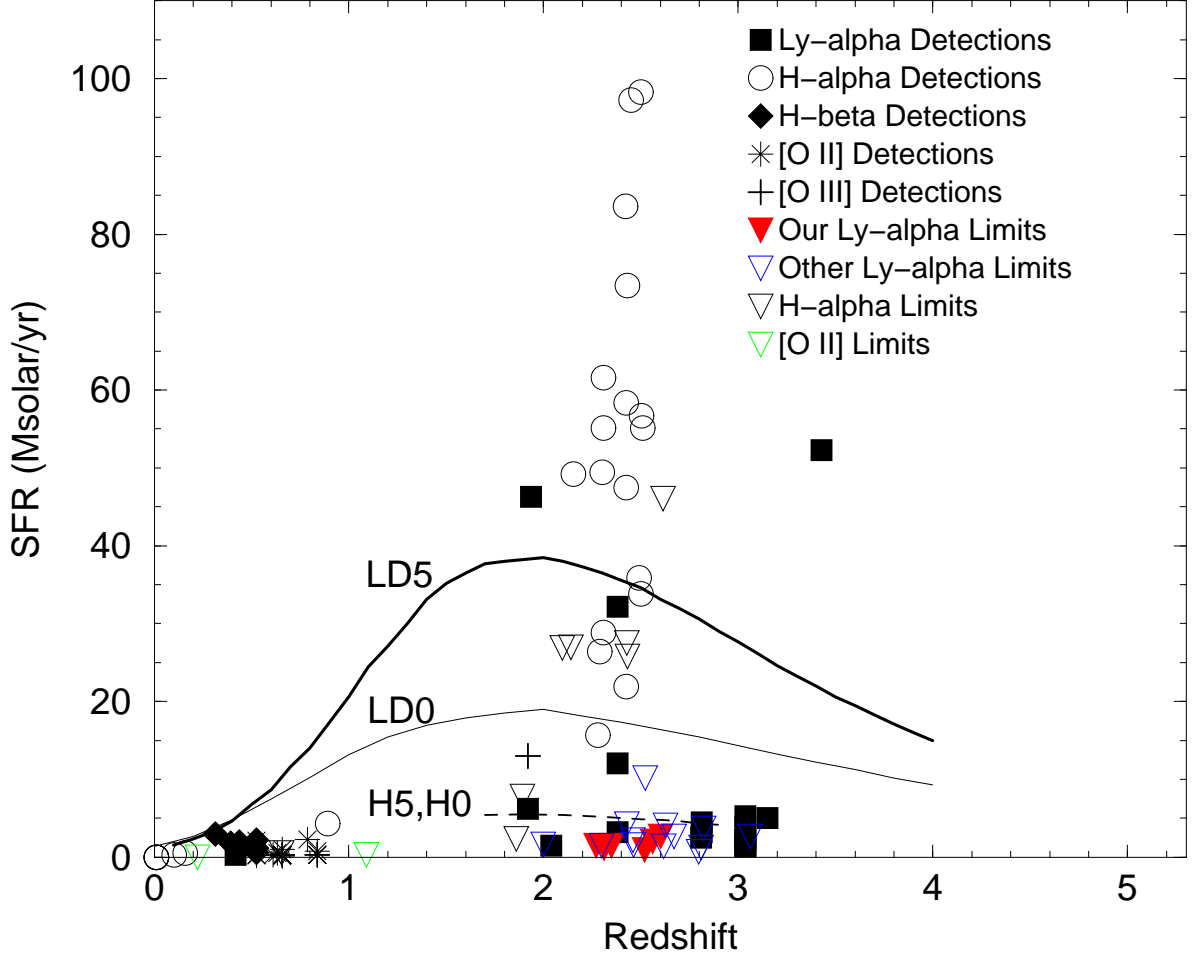
FIG. 8– *Measurements of star formation rates (in $M_\odot$ yr^{-1}) for candidate objects in quasar absorber fields, from narrow-band imaging and spectroscopic searches for Ly-α, H-α, H-β, [O II] and [O III] emission lines. Data points are from our APO Ly-α survey (this work), our previous NICMOS H-α imaging (Kulkarni et al. 2000, 2001), and other literature (see text). Most of the higher values are based on candidate H-α emitters, often located far from the quasar lines of sight. The thick solid (upper) and thin solid (middle) curves show, respectively, the calculations of Bunker et al. (1999) for the predicted cross-section-weighted SFR in the large-disk scenario for $q_0 = 0.5$ and $q_0 = 0$. The dashed curve shows the calculations of Bunker et al. (1999) for the hierarchical scenario for $q_0 = 0.5$ and $q_0 = 0$. All of these curves are based on the closed-box global SFR models of Pei & Fall (1995).*

Table 1: List of Targets

QSO	R.A.(J2000)	Dec.(J2000)	z_{em}	z_{abs}	Known Ions	$W_{\text{Ly}-\alpha}^{\text{rest}}$ (Å)
Q0216+080	02:18:57.3	+08:17:28.0	2.9957	2.2931	CIV,AlIII,AlII, SiII,FeII; DLA	...†
Q0636+680	06:42:04.3	+67:58:35.6	3.1775	2.3112	CIV,CII,AlII	...
Q0956+123	09:58:52.3	+12:02:43.2	3.306	2.3104	CIV,SiIV,AlII	1.42
Q1209+093	12:11:34.9	+09:02:22.8	3.297	2.5822	CIV,AlII,FeII; DLA	21.2
Q1442+101	14:45:16.5	+09:58:36.2	3.535	2.5632	OVI, CIV, SiIV, CIII, SiIII, SiII, OI	1.40
Q2233+131	22:36:19.2	+13:26:20.0	3.2978	2.5537	CIV,CII,SiIV,SiIII, SiII,OI; sub-DLA	5.35
53w002	17:14:14.7	+50:15:29.7	...	...	...	...
(Calibration	...	...	...	...	...	...
Field)	...	...	...	...	...	...

$\dagger$: $\log N_{\text{HI}} = 20.45$.

Table 2.   Journal of Observations

Object	UT Date	UT	$\sec(z)$	Etalon	Filter	λ_{cent}	$t_{\exp}(s)$	Avg. FWHM (Å)
Q0216+080	2001/11/10	05:55:28.87	1.111	Blue	4050/160	4002.2	2400	14.69
...	2001/11/10	06:36:18.15	1.111	Blue	4050/160	4002.2	1200	
...	2001/11/11	05:42:48.66	1.102	Blue	4050/160	4002.2	2400	
...	2001/11/11	06:52:30.75	1.125	Blue	4050/160	4002.2	1660	
...	2001/11/12	05:20:37.43	1.111	Blue	4050/160	4001.3	2400	
...	2001/11/12	06:05:54.94	1.100	Blue	4050/160	4001.3	2400	
...	2001/12/15	03:17:36.77	1.107	Blue	4050/160	4002.2	2400	
...	2001/12/15	04:00:38.97	1.101	Blue	4050/160	4002.2	2400	
...	2001/12/15	04:50:23.34	1.139	Blue	4050/160	4002.2	2400	
...	2001/12/15	05:32:31.49	1.216	Blue	4050/160	4002.2	2400	
...	2002/11/03	06:59:28.92	1.106	Vis-B	4050/160	4008.0	2400	
...	2002/11/03	07:52:40.87	1.163	Vis-B	4050/160	4008.0	2400	
...	2002/11/08	07:42:27.53	1.180	Vis-B	4050/160	4008.0	1800	
...	2000/10/26	05:23:00.92	1.201	...	B	4400	480	
...	2000/10/26	05:32:58.88	1.180	...	B	4400	480	
...	2000/10/26	05:42:02.58	1.164	...	B	4400	480	
...	2000/10/26	05:51:06.28	1.150	...	B	4400	480	
...	2000/10/26	06:00:28.58	1.137	...	B	4400	480	
...	2001/12/15	01:21:29.11	1.338	...	B	4400	300	
...	2001/12/15	01:27:45.25	1.314	...	B	4400	300	
...	2001/12/15	01:34:03.80	1.292	...	B	4400	300	
...	2001/12/15	01:40:22.75	1.272	...	B	4400	300	
...	2001/12/15	01:46:35.10	1.254	...	B	4400	300	
Q0636+680	2000/10/26	10:51:55.81	1.229	Blue	4050/160	4024	2400	14.66
...	2000/10/26	11:33:12.48	1.224	Blue	4050/160	4024	2400	
...	2001/02/22	03:20:22.82	1.225	Blue	4050/160	4024.3	2400	
...	2001/02/22	04:18:32.24	1.232	Blue	4050/160	4024.3	2400	
...	2001/02/22	05:06:11.28	1.260	Blue	4050/160	4024.3	2400	
...	2001/12/15	07:15:20.01	1.236	Blue	4050/160	4024.2	2400	
...	2001/12/15	07:56:38.23	1.224	Blue	4050/160	4024.2	2400	
...	2001/12/15	08:39:13.21	1.228	Blue	4050/160	4024.2	2400	
...	2001/12/15	09:27:39.32	1.252	Blue	4050/160	4024.2	2400	
...	2002/03/12	02:56:26.66	1.228	Blue	4050/160	4024.2	2400	
...	2002/03/12	03:38:47.01	1.247	Blue	4050/160	4024.2	2400	
...	2002/11/03	10:45:35.05	1.224	Vis-B	4050/160	4030.0	2400	
...	2002/11/03	11:29:28.69	1.229	Vis-B	4050/160	4030.0	2400	
...	2002/11/05	09:44:12.32	1.242	Vis-B	4050/160	4030.0	2400	
...	2000/10/26	10:07:53.96	1.251	...	B	4400	480	
...	2000/10/26	10:17:24.49	1.244	...	B	4400	480	
...	2000/10/26	10:26:39.20	1.239	...	B	4400	480	
...	2000/10/26	10:35:43.11	1.235	...	B	4400	480	
...	2001/02/25	05:16:15.67	1.281	...	B	4400	300	

Table 2—Continued

Object	UT Date	UT	sec(z)	Etalon	Filter	$\lambda_{\rm cent}$	$t_{\rm exp}$(s)	Avg. FWHM (Å)
...	2001/02/25	05:22:41.63	1.288	...	B	4400	300	
...	2001/02/25	05:29:27.60	1.296	...	B	4400	300	
Q0956+123	2001/02/22	06:23:39.98	1.077	Blue	4050/160	4023.3	2400	14.79
...	2001/02/22	07:24:08.73	1.078	Blue	4050/160	4023.3	2400	
...	2001/02/22	08:16:52.25	1.135	Blue	4050/160	4023.3	2400	
...	2001/02/22	09:24:17.19	1.312	Blue	4050/160	4023.3	2400	
...	2001/02/25	08:38:17.40	1.204	Blue	4050/160	4023.4	2400	
...	2001/05/22	03:18:47.08	1.258	Blue	4050/160	4023.3	2400	
...	2002/03/12	05:13:05.87	1.078	Blue	4050/160	4023.2	2400	
...	2002/03/12	05:55:28.03	1.071	Blue	4050/160	4023.2	2400	
...	2002/03/12	06:44:56.70	1.104	Blue	4050/160	4023.2	2400	
...	2001/02/25	06:10:45.09	1.078	...	B	4400	300	
...	2001/02/25	06:17:40.16	1.074	...	B	4400	300	
...	2001/02/25	06:24:01.83	1.072	...	B	4400	300	
...	2001/02/25	06:30:58.02	1.070	...	B	4400	300	
...	2001/02/25	06:37:32.38	1.069	...	B	4400	300	
...	2001/02/25	06:49:41.66	1.069	...	B	4400	300	
...	2001/02/25	07:06:17.69	1.074	...	B	4400	300	
...	2001/02/25	07:12:54.06	1.078	...	B	4400	300	
Q1209+093	2001/05/20	04:42:28.87	1.154	Blue	4300/135	4353.6	2400	7.01
...	2001/05/20	05:28:37.23	1.260	Blue	4300/135	4353.6	2400	
...	2001/05/22	05:11:26.45	1.233	Blue	4300/135	4353.5	2400	
...	2001/05/23	03:41:53.18	1.101	Blue	4300/135	4353.7	2400	
...	2001/05/23	04:24:29.14	1.145	Blue	4300/135	4353.6	2400	
...	2002/03/11	08:52:16.27	1.119	Blue	4300/135	4353.5	2400	
...	2002/03/12	08:25:38.11	1.101	Blue	4300/135	4353.5	2400	
...	2002/03/12	09:17:40.82	1.159	Blue	4300/135	4353.5	2400	
...	2001/05/23	05:22:34.56	1.277	...	B	4400	300	
...	2001/05/23	05:37:57.81	1.332	...	B	4400	300	
...	2001/05/23	05:44:12.36	1.357	...	B	4400	300	
...	2001/05/23	05:50:36.43	1.384	...	B	4400	300	
...	2001/05/23	05:56:55.87	1.413	...	B	4400	300	
...	2001/05/23	06:03:07.01	1.444	...	B	4400	300	
...	2001/05/23	06:09:17.35	1.477	...	B	4400	300	
...	2001/05/23	06:15:38.11	1.514	...	B	4400	300	
Q1442+101	2001/05/20	07:29:32.74	1.170	Blue	4300/135	4330.5	2400	6.10
...	2001/05/20	08:17:28.39	1.299	Blue	4300/135	4330.4	2400	
...	2001/05/21	06:37:53.56	1.104	Blue	4300/135	4330.6	2400	
...	2001/05/21	07:27:17.70	1.174	Blue	4300/135	4330.5	2400	

Table 2—Continued

Object	UT Date	UT	sec(z)	Etalon	Filter	$\lambda_{\rm cent}$	$t_{\rm exp}$(s)	Avg. FWHM (Å)
...	2001/05/21	08:09:09.42	1.284	Blue	4300/135	4330.4	2400	
...	2001/05/22	06:15:29.60	1.091	Blue	4300/135	4330.5	2400	
...	2001/05/22	06:57:37.14	1.130	Blue	4300/135	4330.5	2400	
...	2001/05/23	06:51:26.89	1.127	Blue	4300/135	4330.5	2400	
...	2001/05/23	07:33:07.00	1.204	Blue	4300/135	4330.5	2400	
...	2001/02/25	10:03:28.53	1.153	...	B	4400	300	
...	2001/02/25	10:10:44.33	1.141	...	B	4400	300	
...	2001/02/25	10:18:19.75	1.130	...	B	4400	300	
...	2001/02/25	10:26:38.82	1.120	...	B	4400	300	
...	2001/02/25	11:21:21.65	1.085	...	B	4400	300	
...	2001/02/25	11:32:29.47	1.085	...	B	4400	300	
...	2001/02/25	11:41:09.15	1.087	...	B	4400	300	
...	2001/02/25	11:48:41.57	1.089	...	B	4400	300	
...	2001/02/25	11:55:50.50	1.0938	...	B	4400	300	
...	2001/05/23	08:21:14.63	1.359	...	B	4400	300	
...	2001/05/23	08:27:35.43	1.387	...	B	4400	300	
...	2001/05/23	08:33:59.98	1.418	...	B	4400	300	
Q2233+131	2000/10/26	03:45:44.77	1.066	Blue	4300/135	4319	2400	5.59
...	2000/10/27	01:38:14.59	1.150	Blue	4300/135	4314.3	2400	
...	2000/10/27	02:41:43.61	1.070	Blue	4300/135	4317.0	2400	
...	2000/10/27	03:32:30.68	1.062	Blue	4300/135	4318	2400	
...	2000/10/27	04:20:34.25	1.097	Blue	4300/135	4318	2400	
...	2000/10/27	05:12:21.30	1.190	Blue	4300/135	4318.5	2400	
...	2000/10/27	06:11:24.96	1.398	Blue	4300/135	4319	2400	
...	2001/11/10	02:29:02.38	1.060	Blue	4313/116	4318.9	2400	
...	2001/11/10	03:10:40.90	1.081	Blue	4313/116	4318.9	2400	
...	2001/11/10	03:52:49.45	1.136	Blue	4313/116	4318.9	2400	
...	2001/11/10	04:34:24.56	1.233	Blue	4313/116	4318.9	2400	
...	2001/11/11	02:01:10.21	1.062	Blue	4313/116	4318.9	2400	
...	2001/11/11	02:45:46.09	1.066	Blue	4313/116	4318.9	2400	
...	2001/11/12	02:18:11.07	1.060	Blue	4313/116	4318.9	2400	
...	2001/11/12	03:01:43.69	1.080	Blue	4313/116	4318.9	2400	
...	2002/11/04	03:08:18.76	1.064	Vis-B	4300/135	4325.0	1740	
...	2002/11/06	01:29:15.00	1.104	Vis-B	4300/135	4325.0	2400	
...	2002/11/06	02:31:17.24	1.060	Vis-B	4300/135	4325.0	800	
...	2002/11/06	05:02:00.19	1.268	Vis-B	4300/135	4325.0	2400	
...	2000/10/26	02:42:34.68	1.072	...	B	4400	480	
...	2000/10/26	02:53:33.87	1.066	...	B	4400	480	
...	2000/10/26	03:06:41.39	1.061	...	B	4400	480	
...	2000/10/26	03:17:01.37	1.060	...	B	4400	480	
...	2000/10/26	03:28:07.59	1.060	...	B	4400	480	
...	2001/11/11	03:54:43.13	1.147	...	B	4400	2400	

Table 2—Continued

Object	UT Date	UT	$\sec(z)$	Etalon	Filter	λ_{cent}	$t_{\exp}(\mathrm{s})$	Avg. FWHM (Å)
...	2000/10/25	05:26:24.96	1.205	...	B	4400	1200	
53w002	2001/05/20	09:45:49.27	1.086	Blue	4155/160	4128.4	2400	8.31
...	2001/05/21	09:34:32.16	1.079	Blue	4155/160	4128.5	2400	
...	2001/05/21	10:15:54.17	1.126	Blue	4155/160	4128.6	2400	
...	2001/05/22	09:08:42.61	1.063	Blue	4155/160	4128.3	2400	
...	2001/05/23	09:31:39.77	1.084	Blue	4155/160	4128.3	2400	
...	2001/05/22	09:57:53.15	1.108	...	B	4400	300	
...	2001/05/22	10:04:47.73	1.117	...	B	4400	300	
...	2001/05/22	10:10:54.66	1.125	...	B	4400	300	
...	2001/05/22	10:17:17.82	1.134	...	B	4400	300	
...	2001/05/22	10:23:55.19	1.145	...	B	4400	300	
...	2001/05/22	10:34:30.57	1.163	...	B	4400	300	
...	2001/05/22	10:41:24.96	1.176	...	B	4400	300	
...	2001/05/22	10:52:14.56	1.197	...	B	4400	300	
...	2001/05/23	08:44:33.56	1.054	...	B	4400	300	
...	2001/05/23	08:51:20.34	1.057	...	B	4400	300	
...	2001/05/23	08:57:47.50	1.060	...	B	4400	300	
...	2001/05/23	09:05:17.92	1.064	...	B	4400	300	

Table 3: Lyman-α Point source flux sensitivities and Constraints on Star Formation Rates

QSO	z_{abs}	$f^{\dagger}_{\mathrm{Ly}-\alpha}(\mathrm{erg\ s^{-1}\ cm^{-2}})$	SFR $(M_{\odot}\ \mathrm{yr}^{-1})^{\dagger\dagger}$
Q0216+080	2.2931	$< 4.0 \times 10^{-17}$	< 1.5
Q0636+680	2.3112	$< 3.2 \times 10^{-17}$	< 1.2
Q0956+123	2.3104	$< 3.9 \times 10^{-17}$	< 1.5
Q1209+093	2.5822	$< 5.4 \times 10^{-17}$	< 2.7
Q1442+101	2.5632	$< 4.2 \times 10^{-17}$	< 2.0
Q2233+131	2.5537	$< 1.9 \times 10^{-17}$	< 0.9

$\dagger$: 3 σ upper limits on Lyman-α flux for a 2 pixel x 2 pixel region, corresponding to a physical size of $6.0h^{-1}$ kpc x 6.0 kpc at $z = 2.4$; $\dagger\dagger$: 3 σ upper limits on SFR.

This figure "f2a.jpg" is available in "jpg" format from:

http://arXiv.org/ps/astro-ph/0509182v1

This figure "f2b.jpg" is available in "jpg" format from:

http://arXiv.org/ps/astro-ph/0509182v1

This figure "f2c.jpg" is available in "jpg" format from:

http://arXiv.org/ps/astro-ph/0509182v1

This figure "f2d.jpg" is available in "jpg" format from:

http://arXiv.org/ps/astro-ph/0509182v1

This figure "f3a.jpg" is available in "jpg" format from:

http://arXiv.org/ps/astro-ph/0509182v1

This figure "f3b.jpg" is available in "jpg" format from:

http://arXiv.org/ps/astro-ph/0509182v1

This figure "f3c.jpg" is available in "jpg" format from:

http://arXiv.org/ps/astro-ph/0509182v1

This figure "f3d.jpg" is available in "jpg" format from:

http://arXiv.org/ps/astro-ph/0509182v1

This figure "f4a.jpg" is available in "jpg" format from:

http://arXiv.org/ps/astro-ph/0509182v1

This figure "f4b.jpg" is available in "jpg" format from:

http://arXiv.org/ps/astro-ph/0509182v1

This figure "f4c.jpg" is available in "jpg" format from:

http://arXiv.org/ps/astro-ph/0509182v1

This figure "f5a.jpg" is available in "jpg" format from:

http://arXiv.org/ps/astro-ph/0509182v1

This figure "f5b.jpg" is available in "jpg" format from:

http://arXiv.org/ps/astro-ph/0509182v1

This figure "f5c.jpg" is available in "jpg" format from:

http://arXiv.org/ps/astro-ph/0509182v1

This figure "f6a.jpg" is available in "jpg" format from:

http://arXiv.org/ps/astro-ph/0509182v1

This figure "f6b.jpg" is available in "jpg" format from:

http://arXiv.org/ps/astro-ph/0509182v1

This figure "f6c.jpg" is available in "jpg" format from:

http://arXiv.org/ps/astro-ph/0509182v1

This figure "f6d.jpg" is available in "jpg" format from:

http://arXiv.org/ps/astro-ph/0509182v1

This figure "f7a.jpg" is available in "jpg" format from:

http://arXiv.org/ps/astro-ph/0509182v1

This figure "f7b.jpg" is available in "jpg" format from:

http://arXiv.org/ps/astro-ph/0509182v1

This figure "f7c.jpg" is available in "jpg" format from:

http://arXiv.org/ps/astro-ph/0509182v1